Effects of dissolved black carbon bound with goethite on physicochemical properties and adsorption capacity for imidacloprid: Adsorption versus coprecipitation

Peng Zhang[1,2]*, Mingming Ma[1,2], Xingying Meng[1,2], Yifei Shao[3] and Aiju Liu[3]*

[1]MOE Key Laboratory of Pollution Processes and Environmental Criteria, College of Environmental Science and Engineering, Nankai University, Tianjin, China, [2]Tianjin Engineering Center of Environmental Diagnosis and Contamination Remediation, Tianjin, China, [3]School of Resources and Environmental Engineering, Shandong University of Technology, Zibo, China

Dissolved black carbon (DBC) is an important component of natural dissolved organic matter and can bind to iron minerals to form DBC-mineral complexes by adsorption and coprecipitation. However, reports regarding the difference in physicochemical properties between adsorbed and coprecipitated DBC-mineral complexes and their sorption capacity for polar organic pollutants are limited. Herein, goethite (Gt) and the adsorbed and coprecipitated complexes of DBC with Gt (SGt-DBC and CGt-DBC) were prepared, and their physicochemical properties and adsorption capacity for polar imidacloprid (IMI) were determined. The results showed that DBC could efficiently bind to Gt by coprecipitation or adsorption, leading to the aggregation of Gt particles, decreasing SSA, and increasing microporous volume, O-containing functional groups and negative charges. A greater effect was observed in CGt-DBC samples than SGt-DBC samples. CGt-DBC samples could more efficiently adsorb IMI than SGt-DBC samples, and CGt-DBC samples obtained the greatest Q_{max} with 68.4 mg/kg. The sorption mechanisms mainly involved hydrophobic partitioning, H-bonding, cation-π and p/π-π electron donor-acceptor interactions and electrostatic interactions. Additionally, the greater solution pH and Na^+ concentration facilitated IMI adsorption on Gt and Gt-DBC samples; however, the Ca^{2+} solution obtained the opposite result. This effect on IMI adsorption was more pronounced for CGt-DBC samples. Therefore, the findings of this study provide a deep understanding of the interactions between Gt and DBC by adsorption and coprecipitation and their effect on the sorption of organic pollutants in natural soil and water environments.

KEYWORDS

dissolved black carbon, goethite, coprecipitation, adsorption, imidacloprid

1 Introduction

Dissolved black carbon (DBC) is an important component of natural dissolved organic matter (NDOM). DBC is derived from the dissolution of black carbon (heterogeneous carbon-rich residues from incomplete combustion of fossil fuels and biomass) in the environment, accounting for approximately 10% of the total NDOM (Jaffe et al., 2013). DBC consists of a concentrated condensed ring matrix and hydrophilic substituents and has high aromaticity and polarity (Liu et al., 2019; Zhang et al., 2020a). Its small aromatic microdomains and abundant oxygen-containing functional groups (OFGs; i.e., -COOH, -C=O, -C-O) can serve as active sites for the adsorption and complexation of pollutants and mediating the environmental transformation process of pollutants, which become the active center of pollutant distribution and transformation in the environment. In recent years, owing to the uniform structures, high aromatic properties and reactivity, the importance of DBC in the soil environment has attracted increasing attention from researchers.

Iron minerals, as an important part of soil minerals, are typical adsorbents and oxidation/reduction agents in soil environments with electric charges on their surface and have an important impact on carbon cycling and pollutant migration and transformation in soil. It is well documented that a variety of DOM can bind to iron minerals by H-bonding (He et al., 2022), surface complexation (Yang et al., 2021a; Xiaoliang et al., 2021) and electrostatic action (Guo et al., 2014), and then form mineral-DOM complexes in soil and water environments. Based on the binding pathways of iron minerals and DOM, it can be defined as an adsorbed mineral-DOM complex and a coprecipitated mineral-DOM complex. The adsorbed mineral-DOM complex is characterized by DOM molecules adsorbed on the surface of iron minerals. When DOM molecules participated in the formation process of iron minerals, they tend to form the coprecipitated mineral-DOM complex. These above processes make the mineral-DOM complexes an important sink of organic matter for the long-term preservation of organic carbon, and can also accelerate the redox reaction of organics and iron and affect the adsorption behavior of pollutants on the surface of the complexes.

Goethite (α-FeOOH; Gt) is a widely distributed iron mineral in water, soil and sediment environments and has been considered a relatively stable sorbent in the natural environment due to its high specific surface area (SSA), surface charge and abundance of Fe-OH (Coughlin and Stone, 1995; Carvalho Filho et al., 2015). It has been proven that DOM can bind Gt to form the Gt-DOM complex in the formation process of its coprecipitation with Gt or its adsorption on Gt surface, which enhances the hydrophobicity and changes the surface elemental composition and charge of Gt (Gu et al., 1994; Xue et al., 2019; Yang et al., 2021b). This can change the adsorption sites and adsorption capacity of Gt for pollutants

(Mueller, 2015). For instance, the bonded humic acid can reduce the surface electrostatic potential of Gt, which can promote the adsorption of cationic pollutants, i.e., Pb^{2+} and Cu^{2+} (Saito et al., 2005; Orsetti et al., 2006). However, due to the decreased electrostatic potential, the bonded humic acid reduced the adsorption of phosphate anions on Gt due to electrostatic repulsion (Antelo et al., 2007; Fu et al., 2013). In addition to electrostatic interactions, providing or occupying adsorption sites enriched the interaction effects between Gt and pollutants. It has been reported that bonded humic acid can significantly enhance the adsorption capacity of Gt for paraquat and acid MCPA [(4-chloro-2-methylphenoxy)-acetic acid] (Brigante et al., 2010; Iglesias et al., 2010). This was attributed to the fact that humic acid provided large numbers of new adsorption sites for paraquat and MCPA. Moreover, the adsorption capacity of Gt-DOM to pollutants is usually influenced by the bonding form between Gt and DOM (Arroyave et al., 2016; Sodano et al., 2017). Previous studies reported that both adsorbed and coprecipitated complexes between Gt and humic acid could improve their adsorption capacity and adsorption rate to organic pollutants in comparison with pure Gt due to higher organic carbon content and smaller SSA (Mikutta et al., 2014; Du et al., 2018). Thus, these changes in surface charge, SSA, organic carbon and aromaticity caused by the bonded DOM alter the adsorption of organic pollutants by Gt. DBC mainly contains fulvic acid and humic acid and has more uniform structures and higher aromatic properties with greater proportions of abundant polycyclic aromatic hydrocarbons, aliphatic carbon and carboxyl carbon in comparison with NDOM. Nuclear magnetic resonance analysis showed that there were highly substituted aromatic microdomains at the molecular edges of DBC, and the substituents were mainly carboxyl and phenolic hydroxyl groups. Owing to the unique molecular structures with highly aromatic properties and abundant aromatic microdomains and OFGs, we can certainly deduce that DBC may be efficiently adsorbed by Gt *via* H-bonding and electrostatic interactions. However, further research is needed to confirm this hypothesis.

Imidacloprid (IMI) is the most widely used neonicotinoid insecticide (Bass et al., 2015), but its high environmental migration ability makes it often detected in the water and soil environment, which poses a threat to environmental ecology (Morrissey et al., 2015). Previous studies showed that IMI prefers to bind with organic matter and mineral components in soil by hydrophobic partition, H-bonding, pore filling, cation-π electron donor-acceptor (EDA) interactions and electrostatic effects (Brozníc et al., 2012; Satkowski et al., 2018; Zheng et al., 2021). However, there are few reports on the adsorption of complexes of Gt and DBC (Gt-DBC) for IMI. We can speculate that the DBC bonded by adsorption and coprecipitation can significantly change the surface OFGs, aromaticity and charge potential of Gt and then influence the adsorption of Gt for IMI.

Hence, a comprehensive study on the morphology, composition and physicochemical properties of adsorbed and coprecipitated Gt-DBC complexes and their adsorption for IMI and the mechanism was conducted to obtain more complete knowledge of the effect of the interactions between Gt and DBC by adsorption and coprecipitation on polar pesticide adsorption. The aims of this paper were to 1) investigate the morphology, composition and physicochemical properties of adsorbed and coprecipitated Gt-DBC complexes; 2) evaluate the adsorption capacity and mechanism of IMI on Gt and adsorbed and coprecipitated Gt-DBC complexes; and 3) investigate the effects of environmental factors (e.g., pH and ion species and strength) on IMI adsorption.

2 Materials and methods

2.1 Biomass and chemicals

Air-dried maize straw was purchased from Tianjin Yader Biological Technology Company (China) and was used for the biochar preparation. The straw was cut into sections 0.1–0.5 cm long. $FeCl_3 \cdot 6H_2O$ and NaOH were obtained from Shanghai Aladdin Reagent Co., Ltd. (China). Acetonitrile was obtained from Tianjin Concord Technology Co., Ltd. (China). The water used in our experiment was deionized with a conductivity less than 18.25 MΩ cm (20°C). Imidacloprid (IMI, 98.5%) purchased from Shandong Sino-Agri United Biotechnology Company (China) was dissolved in acetonitrile for the 5000-mg·L^{-1} stock solution and stored at 4°C for the sorption experiment. The physico-chemical properties of IMI are listed in Supplementary Table S1. All chemicals were used without further purification.

2.2 Preparation of goethite, biochar and dissolved black carbon

Goethite was synthesized according to the method of Lv et al. (2016). Then, 0.5 L of 0.5 M $FeCl_3 \cdot 6H_2O$ was added to 0.4 L of 2.5 M NaOH dropwise in a glass beaker while constantly stirring. The as-synthesized phase precipitate was aged at 70°C for 60 h, centrifuged, washed with deionized water and suspended again. This operation was repeated five times. According to our characterization results of X-ray diffraction (XRD), SSA and TEM (Supplementary Figure S1), the as-synthesized solid iron mineral was identified as Gt (Lv et al., 2016). The Gt suspension was stored at 4°C for the next experiment.

Biochar was prepared by prolyzing maize straw at 400°C for 4 h under oxygen-limited conditions based on our previously reported method (Zhang et al., 2018). The obtained biochar sample was denoted as BC400. DBC was extracted from BC400 according to our previously reported method (Zhang et al., 2020b). The detailed extraction process is shown in Supplementary Text S1. The obtained DBC sample was directly used for total organic carbon (TOC) analysis.

2.3 Preparation of Gt-DBC complexes

Coprecipitated Gt-DBC complexes were prepared by mixing 0.5 L of 0.5 M $FeCl_3$ solution with 0.5 L of 5, 25 and 50 mg·C/L DBC in a glass breaker, respectively, and adding them to 0.4 L of 2.5 M NaOH solution. The obtained precipitate was centrifuged and washed with deionized water 5 times. The solid was collected and stored at 4°C for the next experiment. According to the additive concentrations of DBC, the coprecipitated Gt-DBC complexes were denoted CGt-DBC-5, CGt-DBC-25 and CGt-DBC-50, and their TOC concentrations were 1.67, 3.65 and 7.50 mg·C/g, respectively.

Adsorbed Gt-DBC complexes were prepared by adding 0.4 L of 5 and 50 mg·C/L DBC into 5.6 ml of 0.36 kg/L Gt suspension in a 0.5-L glass breaker, respectively. The pH of the mixture was adjusted to 7.0 ± 0.1. Then, the vial was placed in a shaker and shocked at 25°C and 180 rpm for 48 h, which was confirmed to be a sufficient length of time based on kinetics experiments. After reaching adsorption equilibrium, the vial was centrifuged at 4000 rpm, and the solid was collected and stored at 4°C for the next experiment. According to the additive concentrations of DBC, the adsorbed Gt-DBC complexes were denoted SGt-DBC-5 and SGt-DBC-50, and their TOC concentrations were 0.968 and 4.65 mg·C/g, respectively.

2.4 Characterization

The freshly prepared Gt and Gt-DBC samples were dispersed by ethanol and coated by Au to enhance their conductivity, and then their surface morphology was observed with scanning electron microscopy (SEM, Hitachi S4800, Japan). The crystal structure characterization was analyzed by XRD (D8 Advance, Bruker, Germany). The surface functional groups of the samples were identified by Fourier transform infrared spectroscopy (FTIR, Nicolet iS5, United States) with a mass ratio of sample and KBr of 1: 100 and a scanning range of 4000–400 cm^{-1}. The SSA and porous structure were determined by the Brunauer-Emmett-Teller method (BET, ASAP2460, Micrometrics, United States) and were calculated with the Barrett-Joyner-Halenda (BJH) model. An X-ray photoelectron spectrometer (XPS, ESCALAB 250XI, Thermo Fisher Scientific, United States) was applied to determine the surface elemental composition and functional group contents of the samples (Zhang et al., 2020b). The zeta potential of the sample suspension (100 mg L^{-1}) at pH values of 3–11 was measured using a 90plus Zetasizer (Brookhaven, United States).

2.5 Adsorption experiment

The batch adsorption experiment was conducted in 10-ml gray glass vials containing 0.10 mg adsorbents and 10 ml of 5 mM CaCl₂ background solution. After adding the adsorbent and background solution, the vial was sealed with cap and placed in a shaker at 25.0 ± 1.0°C and 180 rpm to preequilibrate for 2 h. After preequilibration, the designated amount of IMI stock solution was spiked into the vial to achieve concentrations of 2.0 mg/L for the adsorption kinetics and 0.5–3.0 mg/L for the adsorption isotherms. The pH values of the trial suspensions were adjusted to 7.0 ± 0.1 with 0.1 M HCl and NaOH. Each treatment was repeated 3 times. After adsorption, 1.0 ml of suspension was collected at certain time points (0–48 h for adsorption kinetics and 48 h for adsorption isotherms), centrifuged at 12,000 rpm for 5 min and filtered through a 0.22-μm polyethersulfone filter membrane. The filtrate was stored at 4°C for high-performance liquid chromatography (HPLC) analysis. Additionally, the effects of pH values (5–9) and ion species and concentrations (5 and 10 mM NaCl and CaCl₂) on IMI sorption on Gt and Gt-DBC samples were also evaluated in the above adsorption system.

2.6 High-performance liquid chromatography analysis

The HPLC system (Agilent 1200, United States) was equipped with an ultraviolet detector at a wavelength of 254 nm for IMI and a Venusil XBP C18 reversed-phase column (4.6 mm × 250 mm × 5 μm, 150 Å). The mobile phase was acetonitrile:water = 55:45 (V:V) at a flow rate of 1.0 ml/min.

2.7 Data analysis

The adsorption kinetics were fitted by a pseudo-first-order kinetic equation (Eq. 1):

$$ln(Q_e - Q_t) = ln(Q_e) - K_1 t \qquad (1)$$

where Q_t (mg·kg⁻¹) and Q_e (mg·kg⁻¹) are the adsorption concentrations of IMI at time t (h) and equilibrium, respectively, and K_1 (h⁻¹) is the pseudo-first-order kinetic adsorption rate constant.

The sorption isotherms were fitted by the Freundlich model (Eq. 2) and the Langmuir model (Eq. 3):

$$Q_e = K_F C_e^{\frac{1}{n}} \qquad (2)$$

$$Q_e = Q_{max} K_L C_e / (1 + K_L C_e) \qquad (3)$$

where C_e (mg·L⁻¹) and Q_e (mg·kg⁻¹) are the equilibrium concentrations of IMI in the aqueous and solid phases, respectively; K_F [(mg·kg⁻¹)·(mg·L⁻¹)⁻ⁿ] and K_L (L·mg⁻¹) are the

sorption affinities; n is the isotherm nonlinearity index; and Q_{max} (mg·kg⁻¹) is the maximum adsorption amounts of IMI on Gt and Gt-DBC samples.

3 Results and discussion

3.1 Structural characterization of complexes

As shown in Figure 1, SEM images of Gt and Gt-DBC samples indicate that Gt particles presented the typical compact and slender needle-type structure with lengths of 200–400 nm and widths of ~50 nm (Figure 1A). Meanwhile, the flat rodlike structures with lengths of ~500 nm and widths of 200–400 nm appeared in CGt-DBC and SGt-DBC samples (Figures 1B–F). The sizes of these Gt-DBC complexes are similar to those of the Gt-loaded humic acid structures and ferrihydrite-humic acid coprecipitates reported in previous literature (Angelico et al., 2014; Mikutta et al., 2014; Dultz et al., 2018). For CGt-DBC samples, the proportions of flat rodlike structures increased with increasing DBC concentrations (Figures 1B–D), and almost all particles of CGt-DBC-50 showed flat rodlike structures. However, SGt-DBC samples with different DBC additions (5 or 50 mg·C/L) all presented the flat rodlike particles (Figures 1E,F), and some small and slender needle-rod particles appeared in these samples. Such differences may be due to the different combining modes and C/Fe atomic ratios between Gt and DBC in CGt-DBC and SGt-DBC samples (Supplementary Table S2). Previous literature reported that SGt-DBC was formed by the adsorption of organic matter on the surface of pure Gt by polar covalent bonds and electrostatic effects (Kaiser and Guggenberger, 2007). Meanwhile, Gt particles could be agglutinated by DBC and form large aggregations instead of needle-type crystals (Safiur Rahman et al., 2013). These phenomena were observed in the aggregation of organic matter and hematite by Mikutta et al. (2014). However, CGt-DBC was composed of variable mixtures of Gt-DBC complexes and pure Gt, and the formation mechanism mainly included Gt nucleation and crystal growth. When Gt grows larger than the associated organic matter, it will gradually adsorb organic matter to form CGt-DBC (Kleber et al., 2015; Sodano et al., 2017). This may explain the increase in the proportion of flat rodlike structures as the DBC concentration increases on CGt-DBC samples. Additionally, it can be clearly seen that CGt-DBC samples had regular edges and particle shapes and formed some new pores with a greater volume, while more irregular edges appeared in SGt-DBC samples. This is also confirmed by the TEM results of this study (Supplementary Figure S1). This indicates that DBC can agglutinate the Gt particles in the adsorption process and influence the edge and surface roughness of adsorbed Gt-DBC complexes.
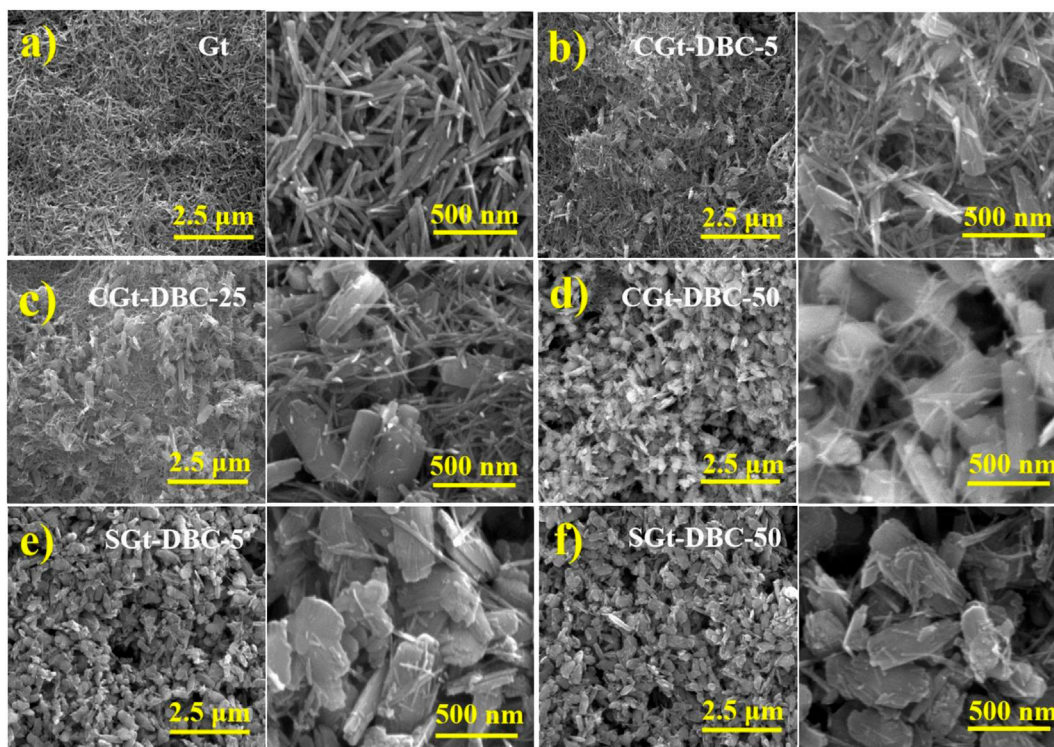
FIGURE 1
SEM images of samples: **(A)** Gt, **(B)** CGt-DBC-5, **(C)** CGt-DBC-25, **(D)** CGt-DBC-50, **(E)** SGt-DBC-5 and **(F)** SGt-DBC-50 (CGt-DBC, the coprecipitated Gt-DBC complexes; SGt-DBC, the adsorbed Gt-DBC complexes; Numbers indicate the additive concentration of DBC in the preparation of Gt-DBC samples).
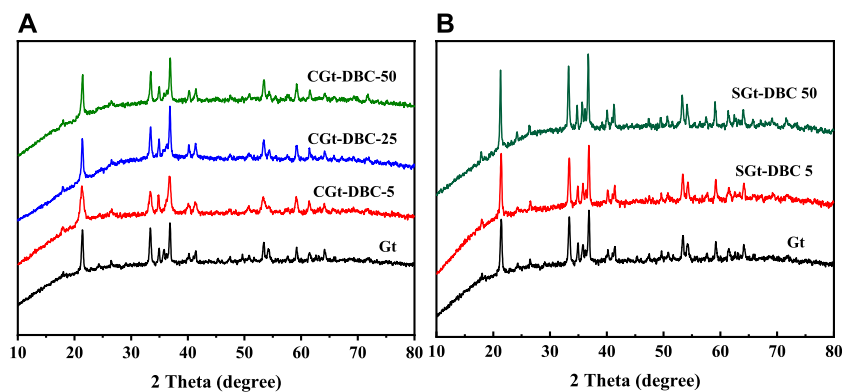
FIGURE 2
XRD patterns of Gt and Gt-DBC samples (CGt-DBC, the coprecipitated Gt-DBC complexes; SGt-DBC, the adsorbed Gt-DBC complexes; Numbers indicate the additive concentration of DBC in the preparation of Gt-DBC samples).

The XRD patterns of Gt and Gt-DBC samples are presented in Figure 2. The distinct peaks at $2\theta = 21.2°$, $33.2°$, $36.7°$, $41.2°$, $53.2°$ and $59.1°$ appearing in the XRD patterns of the Gt and Gt-DBC samples corresponded to the crystal planes of (110), (130) and (111) of Gt, respectively. The different peak intensities at the same peak position between SGt-DBC and Gt samples indicate

FIGURE 3
Nitrogen adsorption-desorption isotherms of Gt and **(A)** CGt-DBC and **(B)** SGt-DBC samples (CGt-DBC, the coprecipitated Gt-DBC complexes; SGt-DBC, the adsorbed Gt-DBC complexes; Numbers indicate the additive concentration of DBC in the preparation of Gt-DBC samples).
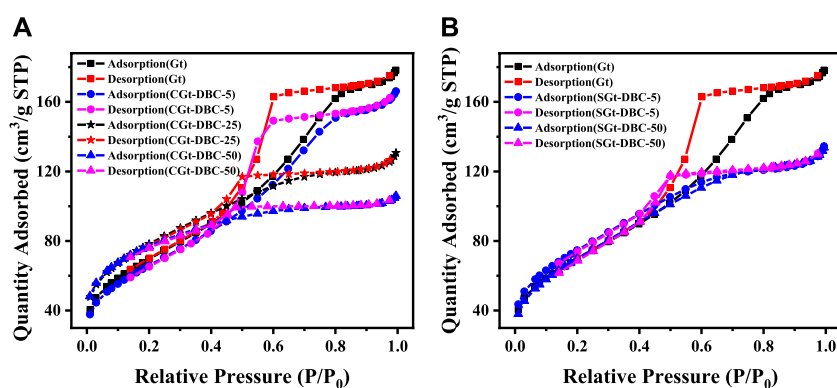
that SGt-DBC samples had better crystallinity (Figure 2B). Furthermore, the absence of the peak at $2\theta = 35.5°$ was observed in the CGt-DBC samples, which suggests that the introduction of DBC leads to the disappearance of the Gt crystal face (Figure 2A). This is similar to the results of previous studies (Schwertmann et al., 2005; Eusterhues et al., 2008). Considering the above SEM result in which the presence of DBC can significantly change the surface morphology of Gt (Figure 1), we speculate that DBC can not only agglutinate the Gt particles by adsorption and coprecipitation but also change the crystal structure of Gt.

The N_2 adsorption-desorption curves of the Gt and Gt-DBC samples are shown in Figure 3. Obviously, the H3-type hysteresis ring presented in the range of $P/P_0 = 0.5–0.8$. Based on the relationship between the hysteresis ring and pore shape, the pore shape of Gt-DBC samples can be defined as cylindrical, and the pore structures were well developed (Alvarez-Torrellas et al., 2016). Furthermore, pure Gt has a greater slope than other adsorbed or coprecipitated Gt-DBC samples when $P/P_0 = 0.5–0.8$. This result suggests that the pore structures caused by the stack of particles in pure Gt are more and smaller than those in the SGt-DBC and CGt-DBC samples, and the increasing DBC concentrations can also enhance the decreasing trend. In particular, the N_2 adsorption curve and desorption curve of the CGt-DBC-50 sample almost overlapped when $P/P_0 = 0.5–0.8$ (Figure 3A). This result suggests that the pores of the CGt-DBC-50 sample with a higher DBC concentration were concave, narrow and semi-enclosed, which are the characteristics of typical capillary pores (Alvarez-Torrellas et al., 2016). Furthermore, the above change in the pore structure of these Gt-DBC samples was also confirmed by the SEM images of this paper (Figure 1). The pore shape decreased with decreasing DBC concentrations in adsorbed or coprecipitated Gt-DBC samples. Notably, these capillary micro- (<2 nm) and mesopore

(2–50 nm) structures in the CGt-DBC-50 sample may more efficiently adsorb the small molecule pesticide IMI by the pore-filling effect than other Gt-DBC and pure Gt samples (Ma et al., 2022). Thus, the complexes formed by Gt adsorbed and coprecipitated with DBC can change the pore structure of Gt-DBC.

The SSA and pore size of the Gt and Gt-DBC samples are listed in Table 1. The SSA of pure Gt is 279.7 m² g⁻¹, which may be due to the surface of nanoscale particles and pores forming from the stack of Gt particles. After adsorption or coprecipitation with DBC, the SSA of the Gt-DBC samples declined by 1.6% for CGt-DBC-5, 12.1% for CGt-DBC-25, 16.9% for CGt-DBC-50, 4.5% for SGt-DBC-5 and 5.4% for SGt-DBC-50. Such declining SSA in Gt-DBC samples may be due to the decrease in quantity of the stackable structures among Gt particles owing to the aggregations and growth of Gt particles caused by the crosslinking with DBC (Figure 1). Furthermore, Mödl et al. (2007) observed that organic matter can cover the surface of Gt and reduce its SSA, which may be another reason for the declining SSA of Gt in this study. Additionally, the results of micropore and mesopore volume (V_{micro} and V_{meso}) and average pore diameter (D_p) of various Gt and Gt-DBC samples showed that compared with pure Gt, Gt adsorbed or coprecipitated with DBC both presented a greater V_{meso} and D_p and lower V_{micro}, especially for CGt-DBC-50. Such differences in Gt and Gt-DBC samples also suggested a positive relationship between the addition concentrations of DBC and the morphological characteristics of Gt-DBC samples (Figure 1 and Table 1). Adsorption and coprecipitation processes all resulted in pore blockage or cover of the Gt surface, but the formation of CGt-DBC samples was accompanied by the formation of Gt, and the DBC and Gt particles coated and bonded layer by layer to form a tight aggregation that N_2 cannot enter. This is different from the fact that the DBC only covers the Gt surface in the SGt-DBC

TABLE 1 Specific surface area and pore structure of Gt and Gt-DBC samples.

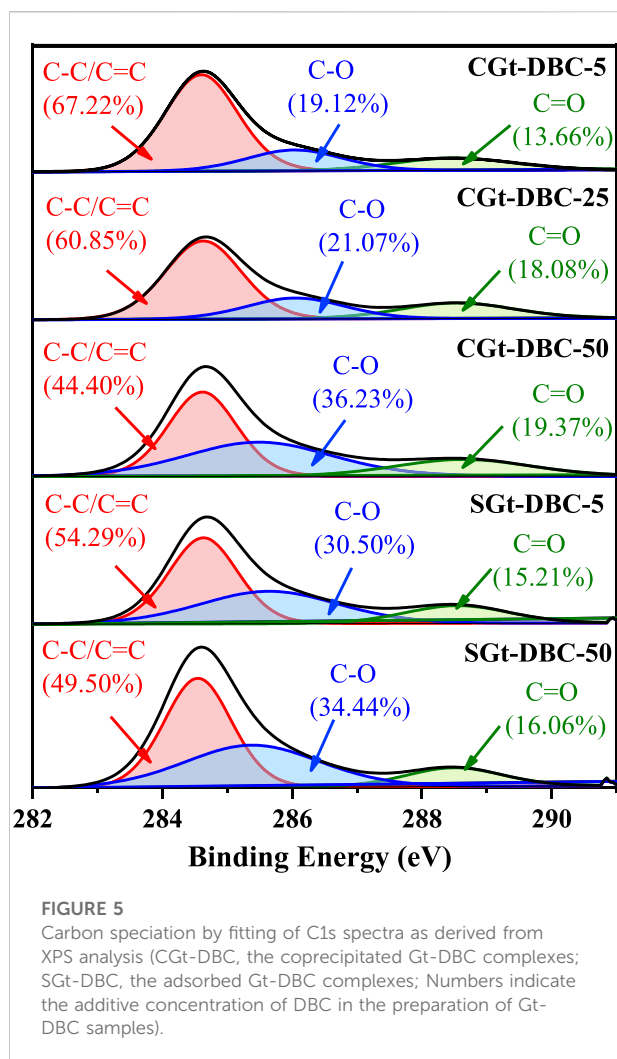| Samples	SSA (m^2 g^{-1})	V_t (cm^3 g^{-1})	V_{micro} (cm^3 g^{-1})	V_{meso} (cm^3 g^{-1})	D_p (nm)
Gt	279.7	0.275	0.072	0.160	2.3
CGt-DBC-5	275.3	0.256	0.062	0.165	2.9
CGt-DBC-25	246.0	0.201	0.042	0.237	4.5
CGt-DBC-50	232.5	0.193	0.038	0.216	4.4
SGt-DBC-5	267.0	0.206	0.065	0.166	3.3
SGt-DBC-50	264.7	0.207	0.055	0.174	3.1

Notes: SSA, V_t, V_{micro}, V_{meso} and D_p represent SSA, total pore volume, micropore volume, mesopore volume and average pore diameter, respectively; CGt-DBC: the coprecipitated Gt-DBC complexes; SGt-DBC: the adsorbed Gt-DBC complexes; Numbers indicate the additive concentration of DBC in the preparation of Gt-DBC samples.

FIGURE 4
FTIR spectra of Gt and Gt-DBC samples (CGt-DBC, the coprecipitated Gt-DBC complexes; SGt-DBC, the adsorbed Gt-DBC complexes; Numbers indicate the additive concentration of DBC in the preparation of Gt-DBC samples).
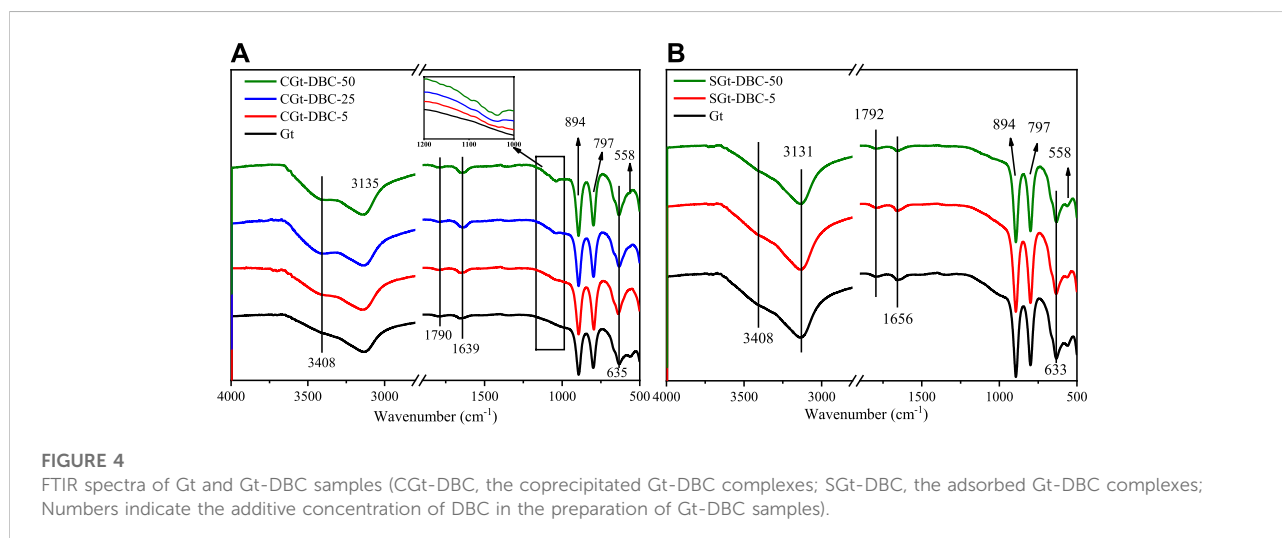
samples; thus, CGt-DBC has a lower SSA than SGt-DBC. The relatively loose needlelike structure of pure Gt can lead to smaller pores and higher porosity, especially providing more micropores. However, the CGt-DBC and SGt-DBC samples contained more large rodlike particles, and their interlacing formed large mesopores (Figure 1). Additionally, Kaiser and Guggenberger (2007) found that DBC could be adsorbed on the Gt surface and block the micropores of Gt, and this is another main reason that the decreasing SSA of the CGt-DBC and SGt-DBC samples of this study. These above reasons can well explain the increasing V_{meso} and declining V_{micro} of CGt-DBC and SGt-DBC samples.

FTIR was applied to determine the surface functional groups of the Gt and Gt-DBC samples. As shown in Figure 4, the FTIR spectrum of pure Gt revealed strong characteristic peaks at 3135, 894, 797 and 633–635 cm^{-1}, corresponding to -OH and Fe-O functional groups, respectively, which was consistent with the FTIR result of Gt reported by Cornell and Schwertmann (2003). Compared with

pure Gt, the FTIR spectra of SGt-DBC samples were similar to those of Gt (Figure 4B). This may be because the coupling DBC concentration on the Gt surface was low (Supplementary Table S2), corresponding to the low density of surface functional groups of adsorbed DBC, which hampers detection of these surface functional groups of adsorbed DBC on the Gt surface by FTIR. However, the FTIR spectra of CGt-DBC samples are significantly different from those of pure Gt (Figure 4A). An obvious peak of -COOH at 1000 to 1100 cm^{-1} was observed in the CGt-DBC samples and became more obvious with increasing DBC concentrations. The increase in this functional group is related to carboxylate-Gt formed by ligand exchange between Gt and the -COOH of DBC (Chen et al., 2014). Furthermore, a distinct -OH stretching band at 3408 cm^{-1} was also observed in the CGt-DBC samples (Szewczuk-Karpisz et al., 2021). This is mainly due to the -OH on DBC binding to the Gt surface. Additionally, the stretching vibration peak of Fe-OH at 558 cm^{-1} vanished in the FTIR spectra of CGt-DBC samples in comparison with pure

FIGURE 5
Carbon speciation by fitting of C1s spectra as derived from XPS analysis (CGt-DBC, the coprecipitated Gt-DBC complexes; SGt-DBC, the adsorbed Gt-DBC complexes; Numbers indicate the additive concentration of DBC in the preparation of Gt-DBC samples).

Gt. This is ascribed to the bonds between Gt and OFGs (e.g., -COOH, -OH, -C-O) in the DBC molecules (Ruan et al., 2002).

The bonding states of C on the surface of Gt-DBC samples were determined by fitting of the C1s peak as derived from XPS detail spectra. As shown in Figure 5, the C1s peak can be resolved into three peaks at 284.6, 285.4 and 289.6 eV, corresponding to C-C/C=C, C-O and C=O functional groups. The relative contents of C-O and C=O functional groups of Gt-DBC samples increased with increasing DBC concentrations. This suggests that OFGs were an important factor governing the sorption of DBC on mineral surfaces. Furthermore, the relative contents of C-O and C=O functional groups of CGt-DBC-5 were lower than those of SGt-DBC-5; however, CGt-DBC-50 was greater than SGt-DBC-50 for the relative contents of C-O and C=O functional groups. Our previous study proved that DBC can be efficiently sorbed by iron hydroxides via hydrophobic partition, H-bonding and electrostatic interactions (Zhang et al., 2020b), but owing to the highly unsaturated compounds and compounds rich in OFGs being preferentially sorbed by iron hydroxides, the molecular fractionation of DBC occurred on iron hydroxides surfaces. This may explain the difference in the relative content of C-O and C=O functional groups between CGt-DBC and SGt-DBC at the different concentration levels of adsorbate in this paper. Notably, the relative contents of C=O of CGt-DBC samples are higher than those of SGt-DBC, which also leads to a greater intensity of the C=O absorption peak at 1000–1100 cm^{-1} in the FTIR spectra of CGt-DBC than SGt-DBC (Figure 4). Additionally, the bulk TOC concentrations of CGt-DBC samples are greater than those of SGt-DBC, especially Gt-DBC-50, which has the highest bulk TOC concentration of 7.50 mg·C/L. This was 61.3% greater than the TOC amount of SGt-DBC-50 (Supplementary Table S3; 4.65 mg·C/L). This was also observed in a study by Eusterhues et al. (2011) in which the bulk TOC concentration of the coprecipitated Ferrihydrite-DOM formed by DOM with higher contents of lignin and rich in aromatic components and Ferrihydrite was much higher than that of adsorbed Ferrihydrite-DOM.

Zeta potentials of Gt and Gt-DBC samples under various pH conditions were determined. As shown in Figure 6, the point of zero charge (pH$_{pzc}$) of pure Gt was 8.54. At pH < 8.54, the protonation reaction gradually occurs on the surface of Gt, and a positive zeta potential is obtained. Meanwhile, the deprotonation reaction occurs at pH > 8.54, leading to a negatively charged surface. The pH$_{pzc}$ of CGt-DBC-5, CGt-DBC-25, CGt-DBC-50, SGt-DBC-5 and SGt-DBC-50 decreased to 8.23, 7.15, 6.48, 8.12, and 7.15, respectively (Figure 6A,B). This indicates that the CGt-DBC and SGt-DBC samples have a lower pH$_{pzc}$ than pure Gt. This declining effect in pH$_{pzc}$ of Gt-DBC samples had a significant positive correlation with DBC concentrations ($p < 0.01$). This may be because the adsorbed and coprecipitated DBC contained abundant OFGs (e.g., -COOH, -OH, -C-O), which had negative charges, thus changing the charge distribution on the Gt surface (Bai et al., 2017). Notably, it can also be found that the pH$_{pzc}$ of coprecipitated CGt-DBC is lower than that of adsorbed SGt-DBC at the same DBC additive concentration. This is mainly because the CGt-DBC sample contained higher concentrations of DBC than the SGt-DBC sample (Supplementary Table S2), which endowed the CGt-DBC sample with a greater proportion of OFGs (i.e., C-O and C=O), thus go a higher degree than SGt-DBC sample (Evanko and Dzombak, 1998; Chandler, 2005).

3.2 Adsorption kinetics of imidacloprid

The nonlinear adsorption kinetics of IMI on Gt and Gt-DBC samples are shown in Figure 7A,B. It can be clearly seen that the adsorption amount of IMI on Gt and Gt-DBC samples increased with the extension of reaction time, and the adsorption process can be divided into two stages: the rapid adsorption stage (0–2 h) and the slow adsorption stage (after 2 h). The adsorption amount
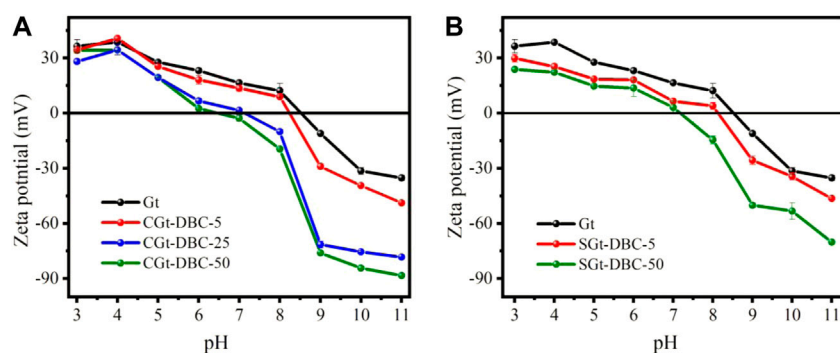
FIGURE 6
Zeta potential of Gt and Gt-DBC samples under different pH conditions (CGt-DBC, the coprecipitated Gt-DBC complexes; SGt-DBC, the adsorbed Gt-DBC complexes; Numbers indicate the additive concentration of DBC in the preparation of Gt-DBC samples).

FIGURE 7
Adsorption kinetics of IMI on Gt and Gt-DBC samples and fitting of pseudo-first-order kinetics model [CGt-DBC, the coprecipitated Gt-DBC complexes; SGt-DBC, the adsorbed Gt-DBC complexes; Numbers indicate the additi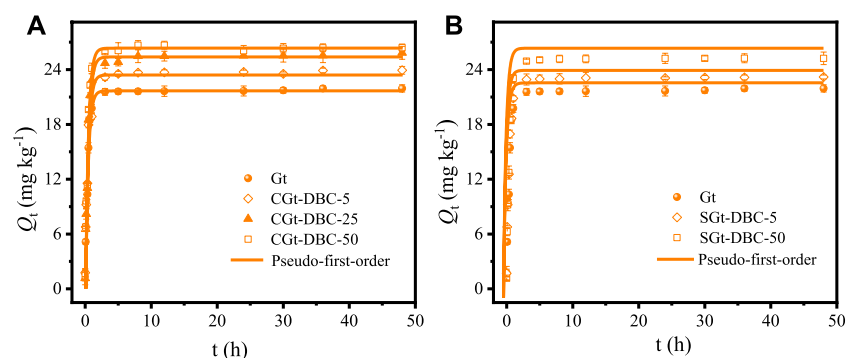ve concentration of DBC in the preparation of Gt-DBC samples; Q_t is the adsorption concentration of IMI at time t (h)].

of IMI during the rapid adsorption stage can account for more than 95% of the equilibrium adsorption amount, which may be due to the abundant active sites (i.e., hydroxyl groups, carboxyl groups (only for Gt-DBC), carbonyl groups (only for Gt-DBC)) on the Gt and Gt-DBC samples for IMI adsorption. In the early adsorption stage, large numbers of adsorption active sites on the surface of these adsorbents, i.e., the external surface of the adsorbents and the inner surface of the micro- and mesopores, can adsorb IMI by the way of single or multiple molecular layers (Sanganyado et al., 2017). After that, the adsorption rate of IMI decreased rapidly, and the adsorption process gradually reached equilibrium and saturation. This was because most of the adsorption sites on the adsorbent surface were occupied in the rapid adsorption process. However, during the slow adsorption process, IMI molecules in the solution began to diffuse into the adsorbent from the outside to the inside, and the mass transfer resistance gradually increased, leading to the

gradual stability of the adsorption amounts of adsorbents for IMI. Thus, the adsorption rate of IMI in the slow adsorption process decreased gradually. According to Sanganyado et al. (2017), this was mainly controlled by the porous internal diffusion of the adsorbents. This phenomenon was also observed in the adsorption of IMI on nanotube composites (Ma et al., 2021), in which more than 80% of IMI adsorbed in the rapid adsorption stage.

The pseudo-first-order model was used to fit the adsorption kinetics. The fitting result showed that the pseudo-first-order kinetics can fit the adsorption curves of IMI on Gt and Gt-DBC samples well (Supplementary Table S3; $R^2 > 0.985$). The theoretical value of Q_e calculated by Eq. 1 was close to the equilibrium adsorption capacity of IMI on these adsorbents in practice (Supplementary Table S3). Compared with pure Gt, the adsorption rate constants (K_1) of CGt-DBC and SGt-DBC samples for IMI all increased. This may be related to the pore
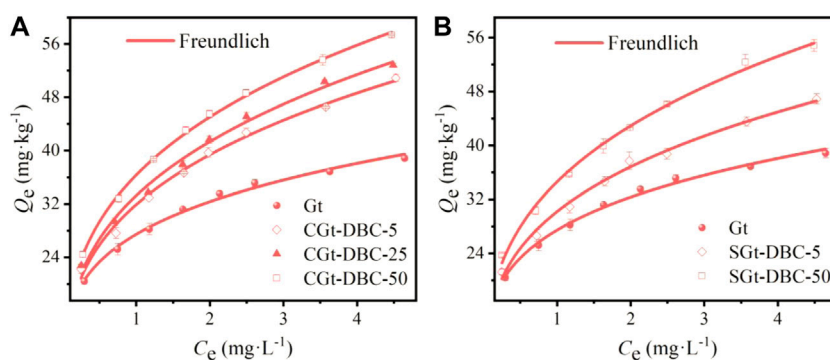
FIGURE 8
Adsorption isotherms of IMI on Gt and Gt-DBC samples and fitting of Freundlich model (CGt-DBC, the coprecipitated Gt-DBC complexes; SGt-DBC, the adsorbed Gt-DBC complexes; Numbers indicate the additive concentration of DBC in the preparation of Gt-DBC samples; Q_e is the equilibrium concentration of IMI in the solid phases).

structure and surface adsorption sites of these adsorbents. Our results above regarding the pore distribution and size of Gt-DBC samples (Table 1) show that Gt-DBC samples had greater V_{meso} and D_p than pure Gt samples, and such changes in the pore quantity and size can enhance the match degree between pore and IMI molecules in size (Supplementary Table S1) and then decrease the mass transfer resistance of IMI to the pore channel. Meanwhile, compared to SGt-DBC samples, the greater V_{meso} and D_p presented in CGt-DBC samples also facilitates overcoming the mass transfer resistance of IMI to the pore channel in CGt-DBC samples. Furthermore, even though the SSA of Gt-DBC samples was significantly reduced, the OFGs (i.e., hydroxyl groups, carboxyl groups, carbonyl groups) and aromatic structures of Gt-DBC samples introduced by adsorption or coprecipitation can provide more adsorption sites for IMI, which may contribute to overcoming the mass transfer resistance of IMI on the adsorbent surface. Additionally, it can be clearly found that the Q_e values of IMI adsorbed on the Gt, CGt-DBC and SGt-DBC samples at equilibrium were in the following order: CGt-DBC-50 > CGt-DBC-25 > SGt-DBC-50 > CGt-DBC-5 > SGt-DBC-5 > pure Gt (Supplementary Table S3). This suggests that CGt-DBC had a stronger adsorption rate and capacity for IMI than pure Gt and SGt-DBC owing to the increased capillary pores with suitable sizes and surface active adsorption sites.

3.3 Adsorption isotherms of imidacloprid

The adsorption isotherms of Gt and Gt-DBC samples for IMI fit all with the Freundlich model well (Figure 8A,B and Supplementary Table S4; $R^2 > 0.991$), and the adsorption of IMI on these materials increased with increasing initial concentrations until saturated adsorption was reached. The Freundlich nonlinear indexes (1/n) of IMI on Gt and Gt-DBC

samples were all less than 1, and the 1/n values of these tested samples were in the order of CGt-DBC-25 ≈ CGt-DBC-50 = SGt-DBC-50 > CGt-DBC-25 > SGt-DBC-5 > pure Gt (Supplementary Table S4). This result suggests that in addition to hydrophobic partition, other adsorption interactions (i.e., H-bonding, pore filling, π-π EDA interactions and electrostatic effects) occurred in the adsorption of IMI on these samples. Meanwhile, the presence of DBC adsorbed and coprecipitated with Gt can enhance the binding capacity of Gt to IMI. Furthermore, the K_F values of IMI adsorption on Gt and Gt-DBC samples were in the order of CGt-DBC-50 > SGt-DBC-50 > CGt-DBC-25 > CGt-DBC-5 > SGt-DBC-5 > pure Gt, and the CGt-DBC-50 sample obtained the greatest K_F value with 36.34 $(mg/kg)/(L/mg)^n$. Notably, under similar additive concentrations of DBC in the preparation process, CGt-DBC showed a stronger adsorption capacity for IMI than SGt-DBC. This may be due to the greater number of surface active adsorption sites (i.e., OFGs) and capillary pores contained in CGt-DBC for IMI adsorption than SGt-DBC. These results indicate that CGt-DBC can more effectively adsorb IMI than pure Gt and SGt-DBC.

To further reveal the main adsorption mechanism of IMI on Gt and Gt-DBC samples, Spearman correlation analysis between K_F, K_d (C_e = 0.5, 5 mg/L) and SSA, V_t, V_{micro}, V_{meso} and D_p was conducted (Supplementary Table S5). The results showed significant negative correlations between K_F, $K_{d, 0.5}$ and $K_{d, 5}$ values and the SSA, V_{micro}, of the adsorbents ($p < 0.05$), while significant positive correlations between V_{meso} and K_F, $K_{d, 0.5}$ and $K_{d, 5}$ values ($p < 0.05$) were observed. After DBC adsorbed on or coprecipitated with Gt, the surface functional groups were altered from the initial Fe-OH to OFGs (i.e., hydroxyl group, carboxyl group, carbonyl group) and aromatic structures, which can form H-bonding, cation-π and p/π-π EDA interactions and electrostatic interactions with the heteroaromatic ring, protonated amine and lone pair electrons in the IMI

molecule. Furthermore, in the adsorption or coprecipitation process, SSA decreased, and new capillary pores formed, indicating an increase in mesopores and increasing D_p of Gt-DBC, which favors the pore-filling effect between IMI and Gt-DBC. These results all contribute to the adsorption of IMI on Gt-DBC. Additionally, to explore the possible effect of porosity and surface sorption sites of Gt and Gt-DBC samples on IMI adsorption, the BET-normalized K_d ($K_{d,BET}$) was calculated (Supplementary Table S6). Obviously, the $K_{d,BET}$ values at $C_e = 0.5$ and 5 mg/L were in the order of CGt-DBC-50 > CGt-DBC-25 > SGt-DBC-50 > CGt-DBC-5 > SGt-DBC-5 > pure Gt. This indicates that in addition to pore filling, other forces such as H-bonding, cation/p/π-π EDA interactions and electrostatic interactions made important contributions to IMI adsorption on Gt and Gt-DBC samples, and these interactions were affected by the DBC concentrations of Gt-DBC.

Many previous studies showed that pure Gt can provide a H-bond donor and positive charge to form H-bonds, cation-π EDA interactions and electrostatic interactions for the adsorption of organic pollutants (Liu et al., 2014; Lee et al., 2017; He et al., 2022). In this study, Cl and N atoms with the lone pair electron and protonated amine of the IMI molecule, acting as H-bond donors (Supplementary Table S1), can form H-bonds with the Fe-OH functional group of Gt. Furthermore, the aromatic heterocycle in the IMI molecule was the π electron acceptor. The presence of -NO$_2$ in the IMI molecule (Supplementary Table S1) can further reduce the heterocyclic electron density to enhance the electron-absorbing ability and enhance the cation-π EDA interaction between Gt and IMI (Zhang et al., 2018). However, the protonated cationic IMI can show electrostatic repulsion with positively charged pure Gt and decrease the adsorption of IMI on pure Gt. Our previous study showed that DBC molecules contain large numbers of OFGs and aromatic structures that interact with IMI by H-bonding, cation-π and p/π-π EDA interactions, and electrostatic interactions (Zhang et al., 2018). After being absorbed on or coprecipitated with Gt, DBC endowed Gt-DBC with more active sites for IMI adsorption, i.e., OFGs, aromatic structures and negative charges (Figures 4-6). The OFGs of Gt-DBC can link with the Cl and N atoms and protonated amine of the IMI molecule by H-bonding, and π electron-rich polyaromatic structures (as π donors) can form cation-π EDA interactions with protonated cationic IMI (Zhang et al., 2018). Furthermore, the Cl and N atoms with the lone pair electron and aromatic heterocycles in IMI molecules can further interact with π electron-rich polyaromatic structures of DBC by the p/π-π EDA interactions (Vijay and Sastry, 2010; Zhang et al., 2013; Xiao and Pignatello, 2015). After adsorbing or coprecipitating with DBC, respectively, CGt-DBC and SGt-DBC samples all showed lower pH_{pzc} values than pure Gt, which will reduce the electrostatic repulsion between the IMI molecule and Gt-DBC. Such decreasing effects in electrostatic repulsion were enhanced with increasing DBC concentrations in

Gt-DBC. Meanwhile, SGt-DBC showed a stronger electrostatic repulsion effect than CGt-DBC. Notably, CGt-DBC-50 decreased to a negative value in pH_{pzc} at the experimental pH (7.0), which endows it with more efficient IMI adsorption by electrostatic interactions. These results can well explain the greater adsorption capacity of IMI on the absorbed and coprecipitated Gt-DBC than pure Gt. Moreover, the characterization results of Gt and Gt-DBC samples obtained in this study indicated greater adsorbed DBC concentrations and OFGs densities and lower pH_{pzc} values in the CGt-DBC samples with higher DBC concentrations than pure Gt and SGt-DBC samples. This may be the main reason that CGt-DBC-50 has the greatest adsorption capacity for IMI.

The maximum adsorption capacity (Q_{max}) of Gt and Gt-DBC samples for IMI was calculated using the Langmuir model. As shown in Supplementary Table S7, the Q_{max} values of these adsorbents for IMI were 38.9 mg/kg for pure Gt, 45.4–49.9 mg/kg for SGt-DBC samples and 53.1–68.4 mg/kg for CGt-DBC samples. The coprecipitated and adsorbed Gt-DBC samples all showed greater Q_{max} values than pure Gt, and the Q_{max} values increased with increasing DBC concentrations. As stated above, in comparison with pure Gt, the newly present OFGs, aromatic structures and capillary pores in coprecipitated and adsorbed Gt-DBC samples can provide more adsorption sites for IMI by H-bonding, cation/p/π-π EDA interactions, pore filling and electrostatic attraction. The enhanced number of OFGs, aromatic structures and capillary pores in the CGt-DBC samples explained their greater Q_{max} values than those of SGt-DBC samples. This result is consistent with the discovery by Du et al. (2018) that the coprecipitated complexes of ferrihydrite and humic acid have a stronger adsorption capacity for pollutants than the adsorbed complexes.

Based on the above results, the adsorbed and coprecipitated Gt-DBC both greatly improved the adsorption capacity for the cationic pesticide IMI compared to pure Gt. The adsorbed and coprecipitated DBC can enhance the electronegativity of Gt and introduce large numbers of OFGs and aromatic structures, which reduce the electrostatic repulsion of IMI and provide large numbers of adsorption sites for IMI through H-bonding and p/π-π EDA interactions. Furthermore, the adsorbed and coprecipitated DBC also changed the pore structure of the Gt-DBC complexes and formed capillary pores, which endowed Gt with adsorption of IMI via the pore-filling effect. In addition, greater DBC concentrations in Gt-DBC samples also led to a stronger adsorption capacity for IMI.

3.4 Effects of environmental factors on adsorption

Environmental factors (i.e., pH, ionic species and strength) are important indices for evaluating the adsorption capacity of adsorbents in the actual environment. In this study, the
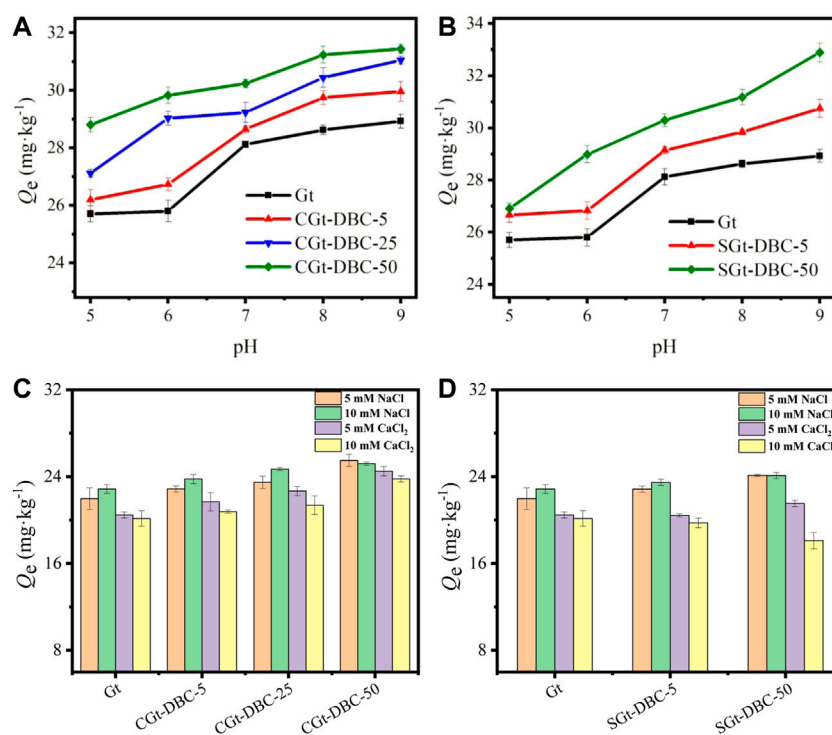
FIGURE 9
Effect of pH **(A,B)** and ionic species and strength **(C,D)** on adsorption of Gt and Gt-DBC samples to imidacloprid (CGt-DBC, the coprecipitated Gt-DBC complexes; SGt-DBC, the adsorbed Gt-DBC complexes; Numbers indicate the additive concentration of DBC in the preparation of Gt-DBC samples; Q_e is the equilibrium concentration of IMI in the solid phases).

background solution adjusted to pH 5-9 or containing 5 and 10 mM Na^+ and Ca^{2+} (pH = 7) was used to evaluate the adsorption performance of Gt and Gt-DBC samples.

3.4.1 pH

The adsorption of IMI on Gt and Gt-DBC samples under different pH conditions was evaluated (Figures 9A,B). The results showed that with increasing pH, the adsorption amounts of IMI on these tested adsorbents all increased. This may be due to the protonation and deprotonation of functional groups (i.e., -OH, -COOH, -NH) of IMI and adsorbents under various solution pH values (Babel and Kurniawan, 2004). When the solution pH is lower than the pH_{pzc} of the adsorbents, the adsorbent surface has a positive charge that interacts with protonated cationic IMI by electrostatic repulsion, thus decreasing IMI adsorption on the adsorbents. With increasing pH, the H^+ concentration in the solution decreased, deprotonation occurred on the adsorbent surface, and the negative charge density increased, which enhanced the electrostatic attraction between protonated cationic IMI and negative adsorbents and then increased their adsorption capacity for IMI (Li et al., 2017; Zhou et al., 2017). Because pH determines the surface charge of Gt and Gt-DBC samples (Geng et al., 2021), the adsorption capacity of these

adsorbents can be improved when pH > pH_{pzc}. Furthermore, the adsorption capacity of IMI in Gt-DBC samples increased in proportion to the concentrations of adsorbed and coprecipitated DBC. This occurred because the higher concentration of adsorbed and coprecipitated DBC introduced more OFGs and capillary pores for new IMI adsorption sites (Figure 6). In addition, previous studies reported that organic pollutant adsorption to Gt at low pH may form complexes on the inner sphere surface (Persson and Axe, 2005; Fu and Quan, 2006), but it may form complexes on the outer sphere surface at high pH (Noren and Persson, 2007). However, this is not observed in this study and needs further research. Thus, a greater solution pH can facilitate the adsorption of IMI to Gt and Gt-DBC samples.

3.4.2 Ionic species and strength

The influence of ionic species and strength on adsorption of Gt and Gt-DBC samples to IMI is presented in Figures 9C,D. It can be clearly seen that ionic species and strength can significantly affect the IMI adsorption to these adsorbents. The adsorption amount of IMI increased with increasing Na^+ concentrations; however, the presence of increasing concentrations of Ca^{2+} obtained the opposite result. A similar phenomenon was observed in a previous study by

Ma et al. (2021). The increase in Na^+ and Ca^{2+} concentrations can also improve the activity coefficient of organic compounds and reduce their solubility through the salting-out effect and then promote IMI adsorption to these Gt and Gt-DBC samples (Bai et al., 2017). Meanwhile, ion species also play an important role in the adsorption process. Researchers proved that a low concentration can promote the adsorption of organic compounds to carbonaceous material, while Ca^{2+} shows strong inhibition due to its competition with tetracycline for surface hydroxyl groups and other adsorption sites (Lin et al., 2017; Dai et al., 2020). In this study, Ca^{2+} can also compete with cationic IMI for adsorption sites (i.e., -OH, -COOH) on the adsorbent surface, which decreases IMI adsorption (Weng et al., 2005). Furthermore, the ionic strength in the solution is too high, and adsorbents and ions may compete for adsorption sites or reduce the adsorption capacity of adsorbents due to the solute saturation effect (Dai et al., 2020). This further explains the declining IMI adsorption on Gt and Gt-DBC samples observed this study in the solution of high Ca^{2+} concentration.

4. Conclusion

The results obtained in the current study suggested that DBC can efficiently and tightly bind with Gt by coprecipitation or adsorption. The presence of DBC promoted the aggregation of Gt particles, and an increase in DBC concentrations further enhanced the aggregation effect for Gt particles. This effect also decreased the SSA and increased the V_{meso}, D_p, OFGs and negative charges of Gt. Furthermore, the complexes of Gt and DBC formed by coprecipitation or adsorption showed significant differences in the morphology, pore structure, SSA, surface functional groups, electric charge and adsorption capacity for IMI. At the same level of C/Fe ratio for the binding process of Gt and DBC, the resulting CGt-DBC samples had more regular flat rodlike structures and OFGs, lower negative charges and formed new capillary pores with a greater volume in comparison with SGt-DBC samples. The adsorption kinetics and sorption isotherms of IMI on Gt-DBC samples were well fitted by a pseudo-first-order kinetic equation and the Freundlich model, respectively. CGt-DBC-50 obtained the greatest Q_{max} with 68.4 mg/kg, which was significantly higher than that of the SGt-DBC and Gt samples. The sorption of IMI on Gt-DBC and Gt samples mainly depended on hydrophobic partitioning, H-bonding, cation-π and p/π-π EDA interactions and electrostatic interactions, and the increasing V_{meso}, D_p, OFGs and negative charges caused by coprecipitated DBC can more greatly enhance IMI sorption on Gt-DBC samples. Additionally, the greater solution pH and Na^+ concentration can facilitate the adsorption of IMI on Gt and Gt-DBC samples. However, the solution of high Ca^{2+} concentration decreased the IMI adsorption on Gt and Gt-DBC samples due to the change in electronegativity of the adsorbent and salting-out effect. This effect on the sorption of IMI can be enhanced in the CGt-DBC samples. Thus, we conclude that the findings of this study provide a deep understanding of the interactions between Gt

and DBC by adsorption and coprecipitation and their effect on the sorption of organic pollutants in natural soil and water environments.

Data availability statement

The original contributions presented in the study are included in the article/Supplementary Material, further inquiries can be directed to the corresponding authors.

Author contributions

PZ: conceptualization, methodology, investigation, and writing-review and editing, and funding acquisition. MM, XM, and YS: conceptualization, methodology, investigation, and writing-original draft. AL: conceptualization, writing-review and editing, and funding acquisition. All authors provided commentary on the study.

Funding

Conflict of interest

The authors declare that the research was conducted in the absence of any commercial or financial relationships that could be construed as a potential conflict of interest.

Publisher's note

All claims expressed in this article are solely those of the authors and do not necessarily represent those of their affiliated organizations, or those of the publisher, the editors and the reviewers. Any product that may be evaluated in this article, or claim that may be made by its manufacturer, is not guaranteed or endorsed by the publisher.

Supplementary material

The Supplementary Material for this article can be found online at: https://www.frontiersin.org/articles/10.3389/fenvs.2022.1013282/full#supplementary-material

References

Alvarez-Torrellas, S., Munoz, M., Zazo, J. A., Casas, J. A., and Garcia, J. (2016). Synthesis of high surface area carbon adsorbents prepared from pine sawdust-Onopordum acanthium L. for nonsteroidal anti-inflammatory drugs adsorption. *J. Environ. Manage.* 183, 294–305. doi:10.1016/j.jenvman.2016.08.077

Angelico, R., Ceglie, A., He, J-Z., Liu, Y-R., Palumbo, G., and Colombo, C. (2014). Particle size, charge and colloidal stability of humic acids coprecipitated with Ferrihydrite. *Chemosphere* 99, 239–247. doi:10.1016/j.chemosphere.2013.10.092

Antelo, J., Arce, F., Avena, M., Fiol, S., López, R., and Macías, F. (2007). Adsorption of a soil humic acid at the surface of goethite and its competitive interaction with phosphate. *Geoderma* 138, 12–19. doi:10.1016/j.geoderma.2006.10.011

Arroyave, J. M., Waiman, C. C., Zanini, G. P., and Avena, M. J. (2016). Effect of humic acid on the adsorption/desorption behavior of glyphosate on goethite. Isotherms and kinetics. *Chemosphere* 145, 34–41. doi:10.1016/j.chemosphere.2015.11.082

Babel, S., and Kurniawan, T. A. (2004). Cr(VI) removal from synthetic wastewater using coconut shell charcoal and commercial activated carbon modified with oxidizing agents and/or chitosan. *Chemosphere* 54, 951–967. doi:10.1016/j.chemosphere.2003.10.001

Bai, L., Cao, C., Wang, C., Wang, C., Zhang, H., and Jiang, H. (2017). Roles of phytoplankton- and macrophyte-derived dissolved organic matter in sulfamethazine adsorption on goethite. *Environ. Pollut.* 230, 87–95. doi:10.1016/j.envpol.2017.06.032

Bass, C., Denholm, I., Williamson, M. S., and Nauen, R. (2015). The global status of insect resistance to neonicotinoid insecticides. *Pestic. Biochem. Physiol.* 121, 78–87. doi:10.1016/j.pestbp.2015.04.004

Brigante, M., Zanini, G., and Avena, M. (2010). Effect of humic acids on the adsorption of paraquat by goethite. *J. Hazard. Mat.* 184, 241–247. doi:10.1016/j.jhazmat.2010.08.028

Broznić, D., Marinić, J., Tota, M., Jurešić, G. Č., Petković, O., and Milin, Č. (2012). Hysteretic behavior of imidacloprid sorption-desorption in soils of Croatian coastal regions. *Soil Sediment Contam. Int. J.* 21, 850–871. doi:10.1080/15320383.2012.697934

Carvalho Filho, A. D., Inda, A. V., Fink, J. R., and Curi, N. (2015). Iron oxides in soils of different lithological origins in Ferriferous Quadrilateral (Minas Gerais, Brazil). *Appl. Clay Sci.* 118, 1–7. doi:10.1016/j.clay.2015.08.037

Chandler, D. (2005). Interfaces and the driving force of hydrophobic assembly. *Nature* 437, 640–647. doi:10.1038/nature04162

Chen, C., Dynes, J. J., Wang, J., and Sparks, D. L. (2014). Properties of Fe-organic matter associations via coprecipitation versus adsorption. *Environ. Sci. Technol.* 48, 13751–13759. doi:10.1021/es503669u

Cornell, R. M., and Schwertmann, U. (2003). *The iron oxides : Structure, properties, reactions, occurrences, and uses*. Weinheim: Wiley VCH.

Coughlin, B. R., and Stone, A. T. (1995). Nonreversible adsorption of divalent metal ions (MnII, CoII, NiII, CuII, and PbII) onto goethite: Effects of acidification, FeII addition, and picolinic acid addition. *Environ. Sci. Technol.* 29, 2445–2455. doi:10.1021/es00009a042

Dai, J., Meng, X., Zhang, Y., and Huang, Y. (2020). Effects of modification and magnetization of rice straw derived biochar on adsorption of tetracycline from water. *Bioresour. Technol.* 311, 123455. doi:10.1016/j.biortech.2020.123455

Du, H. H., Huang, Q. Y., Lei, M., and Tie, B. Q. (2018). Sorption of Pb(II) by nanosized ferrihydrite organo-mineral composites formed by adsorption versus coprecipitation. *ACS Earth Space Chem.* 2, 556–564. doi:10.1021/acsearthspacechem.8b00005

Dultz, S., Steinke, H., Mikutta, R., Woche, S. K., and Guggenberger, G. (2018). Impact of organic matter types on surface charge and aggregation of goethite. *Colloids Surfaces A Physicochem. Eng. Aspects* 554, 156–168. doi:10.1016/j.colsurfa.2018.06.040

Eusterhues, K., Rennert, T., Knicker, H., Kögel-Knabner, I., Totsche, K., and Schwertmann, U. (2011). Fractionation of organic matter due to reaction with ferrihydrite: Coprecipitation versus adsorption. *Environ. Sci. Technol.* 45, 527–533. doi:10.1021/es1023898

Eusterhues, K., Wagner, F. E., Hausler, W., Hanzlik, M., Knicker, H., Totsche, K. U., et al. (2008). Characterization of ferrihydrite-soil organic matter coprecipitates by X-ray diffraction and Mossbauer spectroscopy. *Environ. Sci. Technol.* 42, 7891–7897. doi:10.1021/es800881w

Evanko, C. R., and Dzombak, D. A. (1998). Influence of structural features on sorption of NOM-analogue organic acids to goethite. *Environ. Sci. Technol.* 32, 2846–2855. doi:10.1021/es980256t

Fu, H., and Quan, X. (2006). Complexes of fulvic acid on the surface of hematite, goethite, and akakaneite: FTIR observation. *Chemosphere* 63, 403–410. doi:10.1016/j.chemosphere.2005.08.054

Fu, Z. Y., Wu, F. C., Song, K., Lin, Y., Bai, Y. C., Zhu, Y. R., et al. (2013). Competitive interaction between soil-derived humic acid and phosphate on goethite. *Appl. Geochem.* 36, 125–131. doi:10.1016/j.apgeochem.2013.05.015

Geng, X., Lv, S., Yang, J., Cui, S., and Zhao, Z. (2021). Carboxyl-functionalized biochar derived from walnut shells with enhanced aqueous adsorption of sulfonamide antibiotics. *J. Environ. Manage.* 280, 111749. doi:10.1016/j.jenvman.2020.111749

Gu, B., Schmitt, J., Chen, Z., Liang, L., and McCarthy, J. F. (1994). Adsorption and desorption of natural organic matter on iron oxide: Mechanisms and models. *Environ. Sci. Technol.* 28, 38–46. doi:10.1021/es00050a007

Guo, X., Yang, C., Wu, Y., and Dang, Z. (2014). The influences of pH and ionic strength on the sorption of tylosin on goethite. *Environ. Sci. Pollut. Res.* 21, 2572–2580. doi:10.1007/s11356-013-2174-z

He, J., Yang, C., Deng, Y., Ouyang, Z., Huang, Z., Yang, J., et al. (2022). Mechanistic insights into the environmental fate of tetracycline affected by ferrihydrite: Adsorption versus degradation. *Sci. Total Environ.* 811, 152283. doi:10.1016/j.scitotenv.2021.152283

Iglesias, A., Lopez, R., Gondar, D., Antelo, J., Fiol, S., and Arce, F. (2010). Adsorption of paraquat on goethite and humic acid-coated goethite. *J. Hazard. Mat.* 183, 664–668. doi:10.1016/j.jhazmat.2010.07.077

Jaffe, R., Ding, Y., Niggemann, J., Vahatalo, A. V., Stubbins, A., Spencer, R. G., et al. (2013). Global charcoal mobilization from soils via dissolution and riverine transport to the oceans. *Science* 340, 345–347. doi:10.1126/science.1231476

Kaiser, K., and Guggenberger, G. (2007). Sorptive stabilization of organic matter by microporous goethite: Sorption into small pores vs. surface complexation. *Eur. J. Soil Sci.* 58, 45–59. doi:10.1111/j.1365-2389.2006.00799.x

Kleber, M., Eusterhues, K., Keiluweit, M., Mikutta, C., Mikutta, R., and Nico, P. S. (2015). Chapter one - mineral–organic associations: Formation, properties, and relevance in soil environments, *Adv. Agron.* 130, 1–140. doi:10.1016/bs.agron2014.10.005

Lee, J. H., Choe, Y., and Lee, S. G. (2017). Adhesion mechanism of bisphenol A diglycidyl ether (BADGE) on an α-Fe 2 O 3 (0001) surface. *J. Ind. Eng. Chem.* 53, 62–67. doi:10.1016/j.jiec.2017.03.047

Li, H., Dong, X., da Silva, E. B., de Oliveira, L. M., Chen, Y., and Ma, L. Q. (2017). Mechanisms of metal sorption by biochars: Biochar characteristics and modifications. *Chemosphere* 178, 466–478. doi:10.1016/j.chemosphere.2017.03.072

Lin, J. W., Zhan, Y. H., Wang, H., Chu, M., Wang, C. F., He, Y., et al. (2017). Effect of calcium ion on phosphate adsorption onto hydrous zirconium oxide. *Chem. Eng. J.* 309, 118–129. doi:10.1016/j.cej.2016.10.001

Liu, C. H., Chu, W. Y., Li, H., Boyd, S. A., Teppen, B. J., Mao, J. D., et al. (2019). Quantification and characterization of dissolved organic carbon from biochars. *Geoderma* 335, 161–169. doi:10.1016/j.geoderma.2018.08.019

Liu, H., Chen, T., and Frost, R. L. (2014). An overview of the role of goethite surfaces in the environment. *Chemosphere* 103, 1–11. doi:10.1016/j.chemosphere.2013.11.065

Lv, J., Zhang, S., Wang, S., Luo, L., Cao, D., and Christie, P. (2016). Molecular-scale investigation with ESI-FT-ICR-MS on fractionation of dissolved organic matter induced by adsorption on iron oxyhydroxides. *Environ. Sci. Technol.* 50, 2328–2336. doi:10.1021/acs.est.5b04996

Ma, Y., Chen, S., Qi, Y., Yang, L., Wu, L., He, L., et al. (2022). An efficient, green and sustainable potassium hydroxide activated magnetic corn cob biochar for imidacloprid removal. *Chemosphere* 291, 132707. doi:10.1016/j.chemosphere.2021.132707

Ma, Y., Wu, L., Li, P., Yang, L., He, L., Chen, S., et al. (2021). A novel, efficient and sustainable magnetic sludge biochar modified by graphene oxide for environmental concentration imidacloprid removal. *J. Hazard. Mat.* 407, 124777. doi:10.1016/j.jhazmat.2020.124777

Mikutta, R., Lorenz, D., Guggenberger, G., Haumaier, L., and Freund, A. (2014). Properties and reactivity of Fe-organic matter associations formed by coprecipitation versus adsorption: Clues from arsenate batch adsorption. *Geochim. Cosmochim. Acta* 144, 258–276. doi:10.1016/j.gca.2014.08.026

Mödl, C., Wörmann, H., and Amelung, W. (2007). Contrasting effects of different types of organic material on surface area and microaggregation of goethite. *Geoderma* 141, 167–173. doi:10.1016/j.geoderma.2007.05.003

Morrissey, C., Mineau, P., Devries, J., Sánchez-Bayo, F., Liess, M., Cavallaro, M., et al. (2015). Neonicotinoid contamination of global surface waters and associated risk to aquatic invertebrates: A review. *Environ. Int.* 74, 291–303. doi:10.1016/j.envint.2014.10.024

Mueller, B. (2015). Experimental interactions between clay minerals and bacteria: A review. *Pedosphere* 25, 799–810. doi:10.1016/s1002-0160(15)30061-8

Noren, K., and Persson, P. (2007). Adsorption of monocarboxylates at the water/goethite interface: The importance of hydrogen bonding. *Geochim. Cosmochim. Acta* 71, 5717–5730. doi:10.1016/j.gca.2007.04.037

Orsetti, S., Quiroga Mde, L., and Andrade, E. M. (2006). Binding of Pb(II) in the system humic acid/goethite at acidic pH. *Chemosphere* 65, 2313–2321. doi:10.1016/j.chemosphere.2006.05.009

Persson, P., and Axe, K. (2005). Adsorption of oxalate and malonate at the water-goethite interface: Molecular surface speciation from IR spectroscopy. *Geochim. Cosmochim. Acta* 69, 541–552. doi:10.1016/j.gca.2004.07.009

Ruan, H. D., Frost, R. L., Kloprogge, J. T., and Duong, L. (2002). Infrared spectroscopy of goethite dehydroxylation. II. Effect of aluminium substitution on the behaviour of hydroxyl units. *Spectrochimica Acta Part A Mol. Biomol. Spectrosc.* 58, 479–491. doi:10.1016/s1386-1425(01)00556-x

Safiur, R. M., Whalen, M., and Gagnon, G. A. (2013). Adsorption of dissolved organic matter (DOM) onto the synthetic iron pipe corrosion scales (goethite and magnetite): Effect of pH. *Chem. Eng. J.* 234, 149–157. doi:10.1016/j.cej.2013.08.077

Saito, T., Koopal, L. K., Nagasaki, S., and Tanaka, S. (2005). Analysis of copper binding in the ternary system Cu2+/humic acid/goethite at neutral to acidic pH. *Environ. Sci. Technol.* 39, 4886–4893. doi:10.1021/es0500308

Sanganyado, E., Lu, Z., Fu, Q., Schlenk, D., and Gan, J. (2017). Chiral pharmaceuticals: A review on their environmental occurrence and fate processes. *Water Res.* 124, 527–542. doi:10.1016/j.watres.2017.08.003

Satkowski, L. E., Goyne, K. W., Anderson, S. H., Lerch, R. N., Webb, E. B., and Snow, D. D. (2018). Imidacloprid sorption and transport in cropland, grass buffer, and riparian buffer soils. *Vadose zone J.* 17, 1–12. doi:10.2136/vzj2017.07.0139

Schwertmann, U., Wagner, F., and Knicker, H. (2005). Ferrihydrite-humic associations: Magnetic hyperfine interactions. *Soil Sci. Soc. Am. J.* 69, 1009–1015. doi:10.2136/sssaj2004.0274

Sodano, M., Lerda, C., Nistico, R., Martin, M., Magnacca, G., Celi, L., et al. (2017). Dissolved organic carbon retention by coprecipitation during the oxidation of ferrous iron. *Geoderma* 307, 19–29. doi:10.1016/j.geoderma.2017.07.022

Szewczuk-Karpisz, K., Tomczyk, A., Celinska, M., Sokolowska, Z., and Kusmierz, M. (2021). Carboxin and diuron adsorption mechanism on sunflower husks biochar and goethite in the single/mixed pesticide solutions. *Mater. (Basel)* 14, 2584. doi:10.3390/ma14102584

Vijay, D., and Sastry, G. N. (2010). The cooperativity of cation–π and π–π interactions. *Chem. Phys. Lett.* 485, 235–242. doi:10.1016/j.cplett.2009.12.012

Weng, L. P., Koopal, L. K., Hiemstra, T., Meeussen, J. C. L., and Van Riemsdijk, W. H. (2005). Interactions of calcium and fulvic acid at the goethite-water interface. *Geochim. Cosmochim. Acta* 69, 325–339. doi:10.1016/j.gca.2004.07.002

Xiao, F., and Pignatello, J. J. (2015). Interactions of triazine herbicides with biochar: Steric and electronic effects. *Water Res.* 80, 179–188. doi:10.1016/j.watres.2015.04.040

Xiaoliang, F., Cao, Q., Meng, F., Song, B., Bai, Z., Zhao, Y., et al. (2021). A Fenton-like system of biochar loading Fe-Al layered double hydroxides (FeAl-LDH@BC)/H2O2 for phenol removal. *Chemosphere* 266, 128992. doi:10.1016/j.chemosphere.2020.128992

Xue, Q., Ran, Y., Tan, Y., Peacock, C. L., and Du, H. (2019). Arsenite and arsenate binding to ferrihydrite organo-mineral coprecipitate: Implications for arsenic mobility and fate in natural environments. *Chemosphere* 224, 103–110. doi:10.1016/j.chemosphere.2019.02.118

Yang, F., Chen, Y., Nan, H., Pei, L., Huang, Y., Cao, X., et al. (2021a). Metal chloride-loaded biochar for phosphorus recovery: Noteworthy roles of inherent minerals in precursor. *Chemosphere* 266, 128991. doi:10.1016/j.chemosphere.2020.128991

Yang, F., Xu, Z., Huang, Y., Tsang, D. C. W., Ok, Y. S., Zhao, L., et al. (2021b). Stabilization of dissolvable biochar by soil minerals: Release reduction and organo-mineral complexes formation. *J. Hazard. Mat.* 412, 125213. doi:10.1016/j.jhazmat.2021.125213

Zhang, P., Huang, P., Xu, X., Sun, H., Jiang, B., and Liao, Y. (2020a). Spectroscopic and molecular characterization of biochar-derived dissolved organic matter and the associations with soil microbial responses. *Sci. Total Environ.* 708, 134619. doi:10.1016/j.scitotenv.2019.134619

Zhang, P., Liu, A., Huang, P., Min, L., and Sun, H. (2020b). Sorption and molecular fractionation of biochar-derived dissolved organic matter on ferrihydrite. *J. Hazard. Mat.* 392, 122260. doi:10.1016/j.jhazmat.2020.122260

Zhang, P., Sun, H., Ren, C., Min, L., and Zhang, H. (2018). Sorption mechanisms of neonicotinoids on biochars and the impact of deashing treatments on biochar structure and neonicotinoids sorption. *Environ. Pollut.* 234, 812–820. doi:10.1016/j.envpol.2017.12.013

Zhang, P., Sun, H., Yu, L., and Sun, T. (2013). Adsorption and catalytic hydrolysis of carbaryl and atrazine on pig manure-derived biochars: Impact of structural properties of biochars. *J. Hazard. Mat.* 244, 217–224. doi:10.1016/j.jhazmat.2012.11.046

Zheng, T., Hu, T., Zhang, J., Tang, C., Duan, J., Song, Y., et al. (2021). Dynamics in imidacloprid sorption related to changes of soil organic matter content and quality along a 20-year cultivation chronosequence of citrus orchards. *Environ. Pollut.* 291, 118069. doi:10.1016/j.envpol.2021.118069

Zhou, Y., Liu, X., Xiang, Y., Wang, P., Zhang, J., Zhang, F., et al. (2017). Modification of biochar derived from sawdust and its application in removal of tetracycline and copper from aqueous solution: Adsorption mechanism and modelling. *Bioresour. Technol.* 245, 266–273. doi:10.1016/j.biortech.2017.08.178